Monthly Notices of the ROYAL ASTRONOMICAL SOCIETY

MNRAS **527,** 10425–10439 (2024) https://doi.org/10.1093/mnras/stad3630
Advance Access publication 2024 January 3

Characterization of the repeating FRB 20220912A with the Allen Telescope Array

Sofia Z. Sheikh [1,2,3★] Wael Farah,[1,2★] Alexander W. Pollak [1,2] Andrew P. V. Siemion,[1,2,4,5] Mohammed A. Chamma,[6] Luigi F. Cruz,[1,2] Roy H. Davis,[1] David R. DeBoer,[1,2] Vishal Gajjar,[1,2] Phil Karn,[1] Jamar Kittling,[1,7] Wenbin Lu [8], Mark Masters,[1] Pranav Premnath,[1,9] Sarah Schoultz,[1] Carol Shumaker,[1] Gurmehar Singh[1,10] and Michael Snodgrass[1]

[1]*SETI Institute, 339 Bernardo Ave, Suite 200 Mountain View, CA 94043, USA*
[2]*Berkeley SETI Research Center, University of California, Berkeley, CA 94720, USA*
[3]*Penn State Extraterrestrial Intelligence Center, 525 Davey Laboratory, The Pennsylvania State University, University Park, PA 16802, USA*
[4]*Department of Physics and Astronomy, Schuster Building Oxford Road Manchester M13 9PL, UK*
[5]*Institute of Space Sciences and Astronomy, University of Malta, Msida MSD2080, Malta*
[6]*Department of Physics & Astronomy, McMaster University, 1280 Main Street West, Hamilton, ON L8S 4M1, Canada*
[7]*Department of Astronomy, Wesleyan University, Middletown, CT 06459, USA*
[8]*Departments of Astronomy and Theoretical Astrophysics Center, UC Berkeley, Berkeley, CA 94720, USA*
[9]*Department of Physics & Astronomy, The University of California, Irvine, CA 92697, USA*
[10]*Department of Physics and Astronomy, Purdue University, West Lafayette, IN 47907, USA*

Accepted 2023 November 20. Received 2023 November 17; in original form 2023 May 19

ABSTRACT

FRB 20220912A is a repeating Fast Radio Burst (FRB) that was discovered in Fall 2022 and remained highly active for several months. We report the detection of 35 FRBs from 541 h of follow-up observations of this source using the recently refurbished Allen Telescope Array, covering 1344 MHz of bandwidth primarily centred at 1572 MHz. All 35 FRBs were detected in the lower half of the band with non-detections in the upper half and covered fluences from 4–431 Jy-ms (median = 48.27 Jy-ms). We find consistency with previous repeater studies for a range of spectrotemporal features including: bursts with downward frequency drifting over time; a positive correlation between bandwidth and centre frequency; and a decrease in sub-burst duration over time. We report an apparent decrease in the centre frequency of observed bursts over the two months of the observing campaign (corresponding to a drop of 6.21 ± 0.76 MHz per d). We predict a cut-off fluence for FRB 20220912A of $F_{\rm max} \lesssim 10^4$ Jy-ms, for this source to be consistent with the all-sky rate, and find that FRB 20220912A significantly contributed to the all-sky FRB rate at a level of a few per cent for fluences of ∼100 Jy-ms. Finally, we investigate characteristic time-scales and sub-burst periodicities and find (a) a median inter-subburst time-scale of 5.82 ± 1.16 ms in the multi-component bursts and (b) no evidence of strict periodicity even in the most evenly spaced multi-component burst in the sample. Our results demonstrate the importance of wideband observations of FRBs, and provide an important set of observational parameters against which to compare FRB progenitor and emission mechanism models.

Key words: instrumentation: interferometers – methods: data analysis – radio continuum: transients.

1 INTRODUCTION

Fast Radio Burst (FRBs), subsecond-duration coherent flashes in the radio spectrum that originate at cosmological distances, are one of the most intriguing phenomena in the last decade of time-domain astronomy. FRBs have been detected at radio frequencies from 120 MHz (Pastor-Marazuela et al. 2021) all the way up to 8 GHz (Gajjar et al. 2018; Michilli et al. 2018), with isotropic-equivalent spectral luminosities of 10^{27}–10^{34} erg s^{-1} Hz^{-1} (Nimmo et al. 2022), and excess Dispersion Measures (DMs) (subtracting the Galactic contribution using electron density models) of several tens to a few thousand pc cm^{-3} (Petroff, Hessels & Lorimer 2022). Most FRBs have only been observed a single time, but some, known as 'repeaters', are seen more than once; the repeater fraction is still evolving with more observation, but, at the moment, only 2.6 per cent of Canadian Hydrogen Intensity Mapping Experiment (CHIME) FRB sources have been seen to repeat (CHIME/FRB Collaboration 2023). The first of these repeaters discovered, FRB20121102A (e.g. Scholz et al. 2016; Spitler et al. 2016; Zhang et al. 2018; Gourdji et al. 2019; Hessels et al. 2019; Agarwal et al. 2020; Majid et al. 2020; Pearlman et al. 2020; Li et al. 2021; CHIME/FRB Collaboration 2023) has now produced thousands of recorded bursts across different instruments and frequency ranges. As of the writing

★ E-mail: ssheikh@seti.org (SS); wfarah@seti.org (WF)

of this paper, 46 FRB sources have been confirmed to repeat, the majority of which do not show any burst-to-burst periodicity (though two sources, FRB121102 and FRB180916, show periodic activity windows, e.g. Pilia et al. 2020; CHIME/FRB Collaboration 2020a). Many FRB sources have been precisely localized by interferometric arrays (Bannister et al. 2019; Marcote et al. 2020; Kirsten et al. 2022; Ravi & DSA-110 Collaboration 2023), which provide important clues to the nature of the emitting objects and their host environments. Repeaters are particularly valuable for interrogating the emission mechanism of FRBs, as their bursts can be analysed as a self-contained sample of observational data arising from a single physical object (e.g. Hessels et al. 2019; Li et al. 2021; Chamma et al. 2023; Jahns et al. 2023).

The emission mechanism of FRBs still remains a mystery (for recent reviews, see Cordes & Chatterjee 2019; Zhang 2020; Bailes 2022; Petroff, Hessels & Lorimer 2022), though a consensus is emerging that magnetars are likely responsible for at least a sub-population due to an FRB-like event from a Galactic magnetar (Bochenek et al. 2020; CHIME/FRB Collaboration 2020b). For magnetar-related classes of models, there is still considerable debate on the detailed radiation mechanism, with various explanations distinguished by, among other things, their distance from the progenitor magnetar (Petroff, Hessels & Lorimer 2022). Magnetospheric models operate at a few neutron star radii from the magnetar (e.g. Lu, Kumar & Zhang 2020), while shock models operate much further out, at characteristic scales of 10^{10} cm (e.g. Metzger, Margalit & Sironi 2019). Most radiation mechanism models for repeaters sufficiently explain the broad features of repeating FRB emission (e.g. coherent emission, an energy budget consistent with repeating bursts, non-cataclysmic sources) and therefore will likely be differentiated via more specific spectrotemporal behaviour.

The observed population of repeating FRBs does show consistent spectrotemporal features, such as the tendency of emission from a single burst to decrease in frequency over the duration of the burst, often in discrete steps associated with distinct 'subpulses' or 'sub-bursts' (Hessels et al. 2019). This so-called sad trombone effect, or downward drift, is not an unbreakable rule, however, as others have reported positive drift rates in some bursts (e.g. Kumar et al. 2022; Zhou et al. 2022). For each FRB, features such as the duration, central frequency, frequency extent, and drift rate can be combined with flux and polarization information to reveal consistent properties across bursts and sources. Specific spectrotemporal features such as upward-drifting 'happy trombones', sub-burst periodicities (CHIME/FRB Collaboration 2023), or $<$100 ns sub-burst structure (Majid et al. 2021; Nimmo et al. 2022) might provide the clues necessary to understand the full nature of FRBs. For example, Zhou et al. (2022) notes the similarity of drifting behaviour in FRBs to that of certain pulsars, hinting at a potential similarity in emission mechanism or environment. Similarly, the small emission regions (tens to thousands of meters) implied by $<$100 ns sub-burst structure lends itself to a magnetospheric origin (Nimmo et al. 2022).

On 2022 October 15, a new repeating source, FRB 20220912A, was reported by McKinven & CHIME/FRB Collaboration (2022); nine bursts at 400 MHz were detected by CHIME in a three day period in September 2022. The original detection had inferred J2000 coordinates of RA = 347.29(4)°, Dec = +48.70(3)°. Other Astronomer's Telegrams soon followed, showing detections at *L* band (Herrmann 2022) and an improved localization from the Deep Synoptic Array (DSA-110) at $23^{h}09^{m}04^{s}.9 + 48^{d}42^{m}25^{s}.4$ (J2000) (Ravi 2022). This location is coincident with the potential host galaxy PSO J347.2702+48.7066 (McKinven & CHIME/FRB Collaboration 2022; Ravi 2022). The repeating FRB has since been detected at frequencies from 300 MHz (Bhusare et al. 2022;[1] Fedorova & Rodin 2022) to 2.3 GHz (Perera et al. 2022; Rajwade et al. 2022), with some large single-dish telescopes seeing *L*-band burst rates of over 100 bursts h^{-1} (e.g. Feng et al. 2022). Recent published work on the source in Zhang et al. (2023) and Feng et al. (2023) characterizes this source as the fourth extremely active FRB, but the first one in a relatively clean environment as derived from its polarization information and steady DM, providing a unique laboratory for understanding which FRB properties come from the emission mechanism intrinsically.

Repeating FRBs show varying behaviour across wide bandwidths, for instance, periodicity in activity that is phase-delayed in time over frequency for FRB 20180916B (e.g. Sand et al. 2022). They are also limited in bandwidth (100s of MHz up to a few GHz; e.g. Gourdji et al. 2019) around their unpredictable centre frequencies. Given these characteristics, wide bandwidth receivers and simultaneous observation at different bands will be critical to characterize them. The Allen Telescope Array (ATA) has both of these features, making it a uniquely suited instrument for FRB observation.

In this paper, we report an observing campaign of FRB 20220912A conducted with the ATA between 2022 October and December. In Section 2, we summarize the current status of the refurbishment of the ATA, describe the observational campaign of FRB 20220912A, and detail the search pipeline used to detect and validate FRBs. In Section 3, we discuss our methods for data pre-processing and extraction of spectrotemporal properties. In Section 4, we use the data and properties from the previous section to compute the all-sky rate, quantify correlations between spectrotemporal properties, and investigate potential sub-burst periodicity. Finally, we discuss our results and conclude in Section 5.

2 OBSERVATIONS AND DATA

2.1 The Allen Telescope Array: instrument specifications

The ATA is a 42-element interferometer consisting of 6.1 m dishes hosted on the Hat Creek Radio Observatory in northern California owned and operated by the SETI Institute, Mtn. View, CA. In late 2019, the instrument began a refurbishment programme aimed at improving the sensitivity and robustness of the telescope feeds and revamping the Digital Signal Processing (DSP) system. A full description of the analogue and DSP upgrades will be presented in Pollak et al. (in prep.) and Farah et al. (in prep.) respectively, but here we will include the essential details to accompany the observations of FRB 20220912A.

Each ATA dish is an offset Gregorian and can slew in both the azimuth and elevation direction. The refurbished 'Antonio' log-periodic feeds are dual-polarization and sensitive to a large instantaneous frequency range covering the 1 to 11 GHz band (Welch et al. 2009). Each feed is placed in a cryostat and is cooled to a temperature of ∼70 K. Analogue signals from each antenna are amplified and sent over optical fibre. Each antenna's signal is then split and mixed to produce up to four independently tunable signal chains, denoted 'a', 'b', 'c', and 'd'.

Digitization of the antenna signals is performed on 16-channel input Xilinx ZYNQ UltraScale + Radio Frequency System-on-Chip (RFSoC) boards, where data get channelized, packetized, and transmitted to the network on a 100 GB ethernet link. A delay engine and fringe rotator are also included as part of the firmware on the

[1]There is also a claimed marginal detection at 111 MHz.

Table 1. Specifications of the Allen Telescope Array in Fall 2022.

Parameter	Value
Antenna diameter	6.1 m
Longest baseline	300 m
Frequency coverage	1–11 GHz
Primary beam FWHM (at 1 GHz; at 11 GHz)	3.5°; 0.3°
Synthesized beam FWHM (at 1 GHz; at 11 GHz)	4.2 arcmin; 0.38 arcmin
Processed bandwidth per tuning	672 MHz
Number of available simultaneous tunings	2
Number of simultaneous polarizations	2
Number of beamformed antennas	20

Field Programmable Gate Array boards such that voltage data from all antennas are delayed and phase-centred relative to a user-defined sky coordinate (usually the centre of the ATA antenna primary beam). Five RFSoC boards are currently deployed as part of the prototype DSP system which supports the digitization of 20 dual-polarization antennas over two frequency tunings. Upgrades to outfit the entire ATA with newly refurbished feeds and deploy more digitizers to cover all the available tunings are planned for the near future.

Channelized voltages are received by a cluster of eight compute nodes where data are processed depending on the observer-selected DSP backend. An xGPU-based, which accelerates cross-correlations (x) using Graphical Processing Units (GPUs) (Clark, La Plante & Greenhill 2013), can be selected to generate interferometric visibilities that can be used for imaging and for delay and phase calibrating the beamformer. Our beamformer, Breakthrough Listen Accelerated DSP Engine, is a custom-built GPU-based beamformer that was developed in-house, tested, and deployed on the ATA cluster (Cruz et al., in prep.) and has since been used for novel science, such as tracking the reverse shock emission of gamma-ray burst 221009A (Bright et al. 2023). Telescope users can customize the ATA backend according to science cases. This includes selecting the time-integration length of the correlator, setting the number of beams to produce with the beamformer, and setting the polarization data output.

Table 1 contains a summary of the relevant instrument properties for the FRB observations described here.

2.2 Observing campaign

Just 56 min after the initial announcement of FRB 20220912A by McKinven & CHIME/FRB Collaboration (2022), the ATA began a follow-up campaign of the source. During the time period between 2022 October 15 and 2022 December 31, we observed the source in a series of 70 observations, with a median observation length of 8 h, divided into 30 min scans. This led to a total observing time of 541 h on-source. We ended the campaign when the source's activity had decreased, but not fully ceased, due to observing resource constraints. We recorded data with the 20-element beamformer, placing a single phase-centred synthesized beam on the target at the centre of the primary beam; initially, we used the inferred J2000 coordinates from the CHIME detection of FRB 20220912A, then switched coordinates to the updated DSA-110 coordinates once they were available on 2022 October 25. Given the synthesized beamsize of the ATA at 2 GHz (approximately 2 arcmin), the original FRB coordinates would have placed the true source at the edge of the beamformed beam, which affected the first 31 h of observation. Sheikh et al. (2022) described the detection of eight bursts from FRB 20220912A with the ATA; the eight bursts in that announcement are included in this work.

We exercised the ATA's tuning flexibility to observe the source at two different 672 MHz tunings simultaneously. The centre frequencies of the tunings varied at the beginning of the campaign, but settled at their final values of 1236 and 1908 MHz on 2022 November 4. This setting allows for the two tunings to provide continuous frequency coverage from 900 to 2244 MHz. Before 2022 November 4, 12 sessions had tunings of 1400 and 3000 MHz, 2 sessions had tunings of 1400 and 6000 MHz, and 1 session had tunings of 1150 and 1850 MHz – this amounts to 76/541 h of data recorded at the non-final central frequencies.

Before every observing session, we observed a phase calibrator (3C48, 3C286, or 3C147) in the correlator mode to assess sensitivity and calibrate the instrument with updated delay and phase solutions prior to science observations. In addition, from 2022 November 7 until the end of the campaign, we added an observation of pulsar J0332+5434 for general system validation and validation of the SPANDAK pulse detection pipeline described in Section 2.3.

2.3 Searching for FRBs

The ATA beamformer used for the observations described in the previous section currently produces Stokes I 32-bit SIGPROC 'filterbank'[2] files at a frequency and time resolution of 0.5 MHz and 64μs, respectively. These data were not coherently dedispersed to any particular DM during data-recording, but were stored for off-line FRB searching. The beamformer is capable of producing cross-polarization data products that can enable polarization studies. However, given the intricate nature of polarization calibration, we deliberately chose not to record individual polarizations for this work (though we intend to do so in future studies). Moreover, efforts are currently underway to implement a beamformer mode which supports coherent dedispersion.

In this project, we used the SPANDAK pipeline (Gajjar et al. 2022), which is a wrapper for HEIMDALL, a GPU-accelerated search code for dispersed signals in radio astronomical data (Barsdell 2012). SPANDAK implements additional filtering and candidate evaluation procedures on the HEIMDALL outputs and produces tables of burst candidates along with diagnostic plots that are later visually reviewed by an observer.

We first decimate the filterbank files in bit depth from 32-bit to 8-bit so they are compatible with the existing format requirements for HEIMDALL. We then splice the seven nodes of data for each of the two tunings together, creating one 8-bit filterbank file covering the entirety of the tuning centred at Local Oscillator (LO) b and another covering the entirety of the tuning centred at LOc. Due to the data volume and processing time, we opted not to perform Frequency Interference (RFI) removal before searching.

We assign a DM search range of ±10 per cent from the nominal dispersion measure of 219.46 pc cm^{-3} as reported by the CHIME repeater catalogue[3], with a DM step size calculated such that the Signal-to-Noise Ratio (SNR) loss between DM trials is no more than 0.1 per cent. We then run SPANDAK with an SNR threshold of 10, a boxcar maximum width of 2^{16} samples (4.194 s), and a maximum-candidates-per-second (maxCsec) value of 15, which is slightly higher than the SPANDAK default. The maxCsec parameter is observatory and band dependent as it is strongly correlated

[2] https://sigproc.sourceforge.net/sigproc.pdf
[3] https://www.chime-frb.ca/repeaters

with the RFI environment. For these frequencies at the ATA, we determined that 15 was an appropriate value via test observations of J0332+5434. We execute the search code over each spliced tuning independently, corresponding to a fixed search bandwidth of 672 MHz. The incoherent dedispersion and searching code is then executed and logged. More information about how the SPANDAK candidate plots are constructed can be found in fig. 9 of Gajjar et al. (2021).

The median number of top candidates per observing session was 9, where a top candidate is a HEIMDALL candidate given at least a B–C rank by SPANDAK due to its broad-band characteristics and trial DM-versus-SNR response. The low number of candidates made additional filtering for false-positive RFI unnecessary in most cases.

In 541 h of observation, we detect 35 bursts from FRB 20220912A. All 35 bursts were detected in LOb, the lower 672 MHz tuning, with none detected (or visible simultaneously in dedispersed archives) in LOc. This is consistent with low detection rates at *S* band and non-detections in *C* band (e.g. Kirsten et al. 2022). Dynamic spectra for all the bursts detected with the ATA are shown in Fig. 1. As suggested by the single-tuning detections, the bursts from FRB 20220912A are highly spectrally limited, which was similarly observed in FRB 20180916B (Sand et al. 2022) and FRB 20121102A (Law et al. 2017) – a deeper investigation of spectral extent is performed in Section 4.

The timeline of our detections is visualized in Fig. 2.

3 DATA REDUCTION

3.1 File preparation

Once we have identified an FRB within one of the 30-min long `filterbank` files as described in Section 2.3, we crop the `filterbank` in time, centring on SPANDAK's reported trigger time for the burst. We choose a 10-s cropping length, to capture the entire burst with dispersive delay and provide context for noise and RFI properties.

Next we convert the cropped `filterbanks` to archive files with DSPSR (van Straten & Bailes 2011), using the best-fitting SNR-maximizing DM of the burst from SPANDAK contained in the metadata. This choice visually corresponded with structure-maximizing in the dedispersed waterfall plots for all but two of the bursts. For these two bursts (#24 and #25), we found that the SPANDAK over-disperses the burst, as evidenced by the morphology of the subcomponents and the anomalously large reported DMs (224.94 and 223.24 pc cm^{-3}, respectively). We thus set their archive file DM to the average from the other 33 bursts, at 219.775 pc cm^{-3}. All archive files have the time axis of the file (10 s) read in as 'phase' but are otherwise equivalent to archive files used for other radio pulsar applications.

3.2 Calculating flux and fluence

Using the calibration measurements described in Section 2.2, we calculate the flux and fluence of each of the 35 FRBs in the sample. First, we obtain the System Equivalent Flux Density (SEFD) of each observation. All three flux calibrators in this data set have flux models from Perley & Butler (2017), from which we obtain expected spectral flux densities $S_{\rm exp}$ at the central frequencies of both LOs. We calculate the SEFD for each antenna-polarization combination (antenna x, polarization y) as follows:

$$\mathrm{SEFD}_{x,y} = (G_{\rm cal}^2 \times S_{\rm exp})^{-1}, \quad (1)$$

where $G_{\rm cal}$ is the gain from the associated calibrator file, in units of Jy^{-1}, computed using the Common Astronomy Software Application `gaincal` task (Bean et al. 2022). We then average each of the antenna-polarization SEFDs to get the beamformer SEFD:

$$\mathrm{SEFD}_{\rm beamformer} = \frac{\frac{\Sigma_{x,y}\mathrm{SEFD}_{x,y}}{N_{x,y}}}{N_{\rm el}}, \quad (2)$$

where $N_{x,y} = 40$ (the number of antenna-polarization combinations) and $N_{\rm el} = 20$ (the number of elements in the beamformer). This results in a polarization-averaged $\mathrm{SEFD}_{\rm beamformer}$ of 387 ± 38 Jy. This number is in agreement with earlier tests conducted with the instrument, and details about recovering flux scales and beamformer efficiency for the ATA will be presented in a forthcoming paper (Farah et al., in prep.). For observations listed here, we used a uniform weighting of all antennas for the beamformer.

From this SEFD, we can use the radiometer equation to get the minimum detectable flux density $S_{\nu,\rm min}$ of this work:

$$S_{\nu,\rm min} = \frac{(\mathrm{SNR})(\mathrm{SEFD})}{\sqrt{n_{\rm pol}\tau\,\Delta\nu}}, \quad (3)$$

where τ is the duration of an FRB, $\Delta\nu$ is its frequency extent, and $n_{\rm pol}$ is the number of recorded polarizations (in this case, 2). Therefore, $S_{\nu,\rm min}$ for an SNR threshold of 10, an SEFD of 387 Jy, and a fiducial FRB duration and bandwidth of 1 ms and 672 MHz, is 4.7 Jy.

We detected 35 bursts in 541 h of observing, implying an average burst rate above 4.7 Jy of $6.47^{+1.29}_{-1.09} \times 10^{-2}\,\mathrm{h}^{-1}$, where the uncertainties represent 1-sigma Poisson errors (Gehrels 1986).

We use the Python binding for PSRCHIVE (Hotan, van Straten & Manchester 2004) to load the data as dynamic spectra, incoherently dedisperse each array to the SPANDAK DM described in Section 3.1, and remove the baseline. We then average each array in frequency to get a timeseries burst profile, and normalize it by subtracting the median and dividing by the standard deviation of a noise region consisting of $\pm$1000 time bins (64 ms) on either side of the burst.

At this point, we define the boundaries in the timeseries from which to extract SNRs, fluxes, and fluences. Only seven FRBs consist of a single component; the rest of the sample shows complex sub-burst structure. A sub-burst is qualitatively defined here as a significant local maximum in intensity in an FRB's profile, especially if that structure seems distinct in frequency from the neighbouring emission in the dynamic spectrum. We opt here to measure each of the sub-bursts individually, as not to downweight the flux by averaging over the periods between sub-bursts. The sub-burst delineations determined here are the same ones that are used in the process of extracting spectral properties of sub-bursts, described in Section 3.3.

Using the sub-burst bounds and the normalized profile defined above, we obtain the SNR with $\mathrm{SNR} = \frac{\Sigma p}{\sqrt{N}}$, where p is the normalized profile and N is the number of points across the profile (i.e. the duration of the sub-burst). To transform the SNR into the flux in Jy, we can incorporate the SEFD as follows:

$$S_{\rm Jy} = \frac{\mathrm{SEFD} \times \mathrm{SNR}}{\sqrt{B \times N_{\rm P} \times N \times t_{\rm samp}}} \quad (4)$$

where B is bandwidth of the sub-burst, $N_{\rm P}$ is the number of polarizations, and $t_{\rm samp}$ is the sampling time. Finally, we convert N, the duration in bins, into a duration in ms and multiply by $S_{\rm Jy}$ to get the fluences in Jy-ms.

The SNRs, fluxes, and fluences derived here are included in Table 2 (at the end of the paper). Uncertainties in the DM were derived by applying a sliding boxcar with the parameters used by SPANDAK in the original detection and providing the width of the best-fit

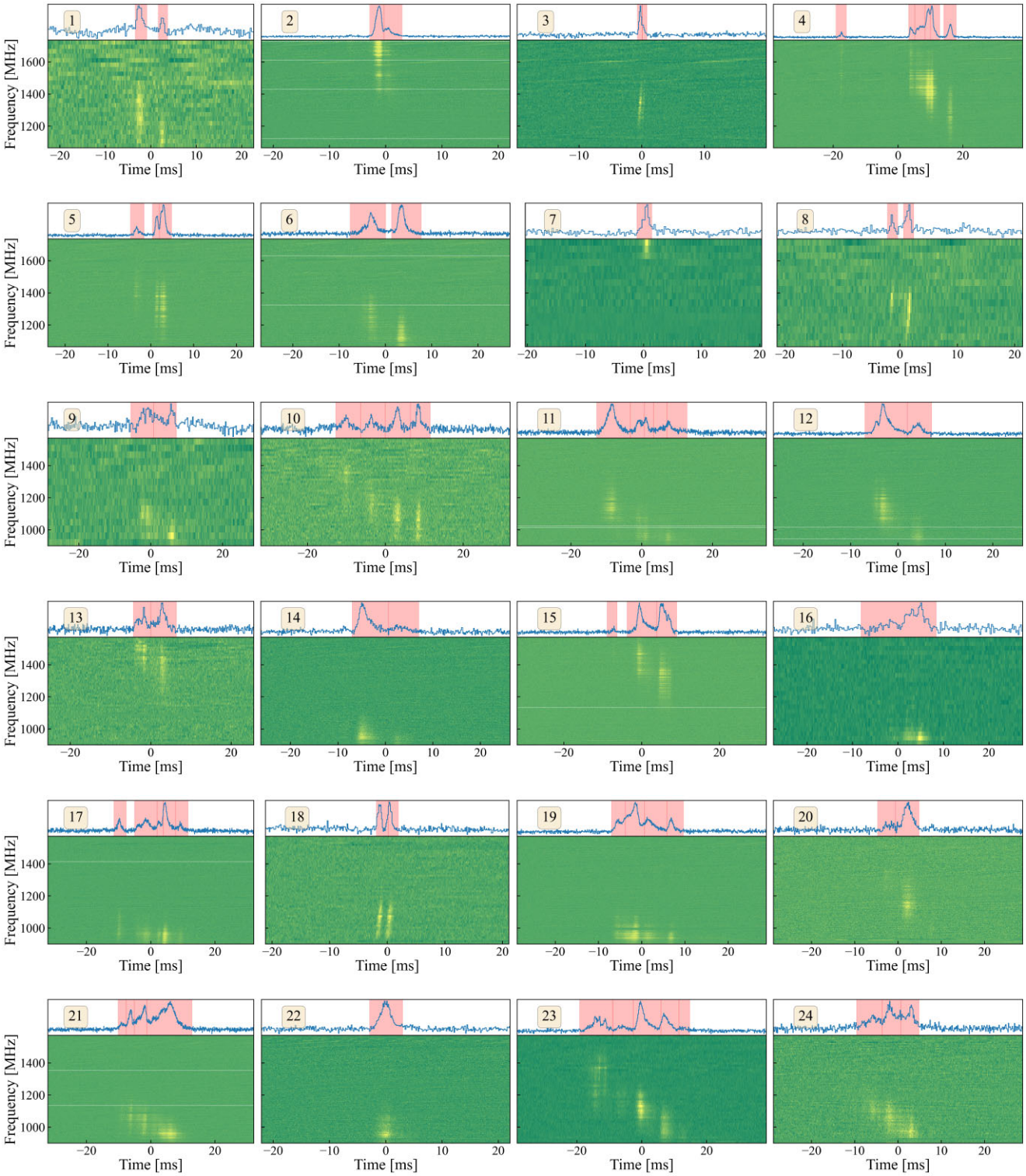

Figure 1. Dynamic spectra (or 'waterfall' plots) for all the bursts from FRB 20220912A detected using the Allen Telescope Array, the frequency-averaged pulse profiles, and the time-averaged spectra. The red-shaded regions in the time series plots denote the time span of the defined sub-bursts, with red vertical lines demarcating adjacent sub-bursts.

Gaussian to the DM–SNR curve. Uncertainties in the fluxes and fluences are calculated by propagating the uncertainty on the mean SEFD.

It should be noted that the first three FRBs in the sample were detected while the synthesized beam was centred on the original, offset coordinates. To address that, we modelled the shape of the synthesized beam at the topocentric coordinates for the aforementioned bursts. We then corrected the measured flux densities with the calculated attenuation values of 0.5, 0.5, and 1 dB for bursts 1, 2, and 3, respectively.

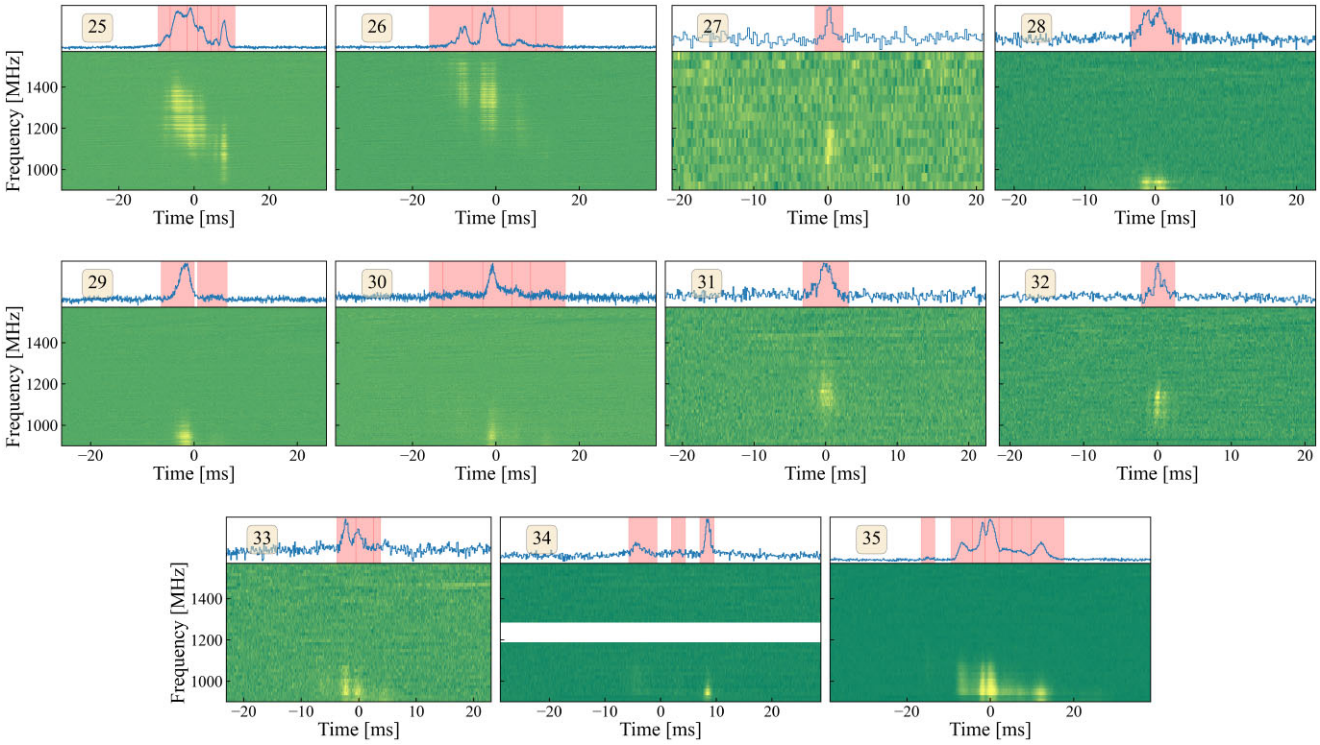

Figure 1. *continued*

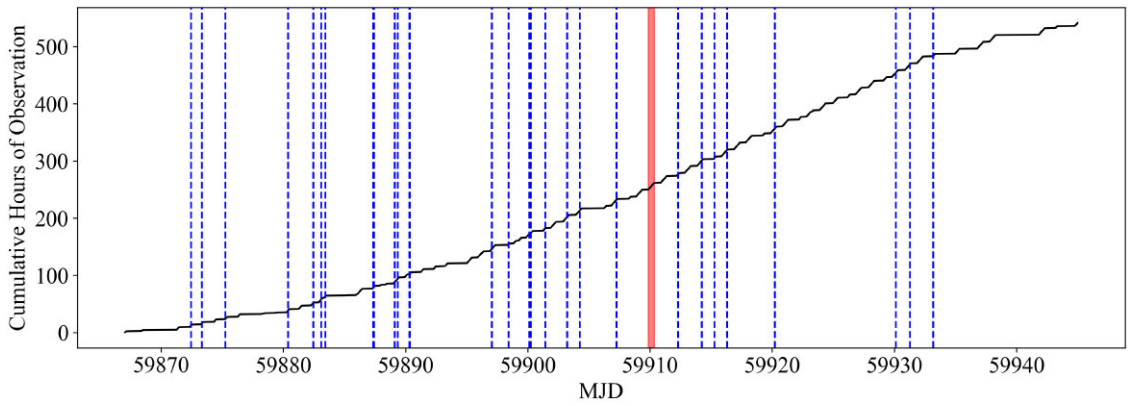

Figure 2. Cumulative observing time on FRB 20220912A over the months of the campaign (black line), with detections marked in dashed blue lines. The red shaded region indicates observations for which the higher tuning was unavailable, restricting our bandwidth by a factor of two. The average interval between observations was 1.11 d, with a maximum interval of 3.80 d and a minimum interval of a few hours.

Some of the flux values in the downsampled 8-bit `filterbank` files were clipped to the highest intensity bin, implying that we were underestimating the total flux by some amount for the brightest FRBs. To estimate the impact of the clipping, we looked at the percentage of pixels in the highest intensity bin for the highest SNR FRB (#25). For this particular FRB, approximately 3 per cent of the pixels were clipped as seen when plotting the pixel intensity distribution histogram. Recovering the original values (i.e. before resizing to 8-bit depth) is almost impossible given that the original 32-bit, higher dynamic range data products were deleted. However, we still attempted to quantify the effects of pixel clipping by assuming that the intensity distribution, at the top end, follows a continuous dampened trend. We fit the intensity histogram, and 'redistribute' the clipped pixels by extrapolating beyond the 8-bit clipping point, and then integrate the intensities and measure the flux. By doing so, we found that we were only underestimating the flux by approximately 3 per cent for this FRB. Given that this is the most extreme example in our sample, we do not correct for this effect in the data set.

3.3 Extracting spectral properties with FRBGUI

Some parameters of interest for the 35 FRB sample are calculated from the original archive files, but some spectrotemporal properties such as bandwidth and duration must be extracted with additional processing, especially for bursts with multiple sub-components. We used the spectrotemporal FRB code FRBGUI (Chamma et al. 2023) to extract these parameters.

We load the archive files into Python, dedisperse, and remove baseline as described in the previous Section 3.2. For each FRB, we defined start time and end time indexes in the original archive file –

Table 2. Properties of the 35 bursts from FRB 20220912A detected by the Allen Telescope Array.

Index	MJD (d)	DM ($pc\,cm^{-3}$)	Width (ms)	Flux (Jy)	Fluence (Jy-ms)	S/N	Centre frequency (MHz)	Bandwidth (MHz)
1	59872.4423299306	219.81 ± 1.22	2.56	6.30 ± 0.57	16.13 ± 1.45	18.53	1289.66 ± 8.39	301.39 ± 0.87
			1.92	3.00 ± 0.27	5.75 ± 0.52	6.08	1220.00 ± 15.03	191.81 ± 2.42
2	59873.3504993634	219.63 ± 1.61	2.56	65.74 ± 5.77	168.30 ± 14.78	177.38	1652.05 ± 4.62	266.21 ± 0.01
			3.20	14.71 ± 1.29	47.04 ± 4.13	53.61	1568.95 ± 4.64	389.06 ± 0.19
3	59875.2672106481	219.46 ± 0.90	0.77	25.60 ± 1.88	19.66 ± 1.45	29.29	1311.63 ± 5.00	227.51 ± 0.35
			0.64	11.26 ± 0.83	7.21 ± 0.53	12.52	1326.39 ± 16.55	257.39 ± 4.28
4	59880.2720233796	219.98 ± 1.95	3.20	5.90 ± 0.59	18.87 ± 1.90	25.10	1545.38 ± 4.69	405.03 ± 0.92
			1.92	25.14 ± 2.53	48.27 ± 4.85	74.93	1491.42 ± 4.65	330.73 ± 0.07
			3.20	44.74 ± 4.50	143.16 ± 14.39	147.75	1453.30 ± 4.62	243.71 ± 0.01
			1.60	108.09 ± 10.86	172.95 ± 17.38	259.44	1427.25 ± 4.62	257.44 ± 0.01
			2.88	59.11 ± 5.94	170.22 ± 17.11	194.19	1418.31 ± 4.62	267.98 ± 0.01
			3.84	21.01 ± 2.11	80.69 ± 8.11	79.35	1280.43 ± 4.62	265.50 ± 0.03
5	59880.3955575231	219.81 ± 1.12	3.20	8.48 ± 0.85	27.12 ± 2.73	29.47	1398.85 ± 4.69	270.24 ± 0.29
			1.60	24.64 ± 2.48	39.42 ± 3.96	63.59	1318.60 ± 4.63	297.62 ± 0.08
			2.88	35.13 ± 3.53	101.18 ± 10.17	122.56	1304.51 ± 4.62	302.13 ± 0.02
6	59880.4029308449	219.78 ± 1.82	7.68	12.60 ± 1.27	96.78 ± 9.73	65.43	1236.88 ± 2.32	250.98 ± 0.02
			6.40	19.80 ± 1.99	126.70 ± 12.73	79.22	1136.83 ± 2.31	178.88 ± 0.01
7	59882.2707171412	219.72 ± 1.43	2.56	9.43 ± 0.94	24.15 ± 2.40	18.76	1683.63 ± 4.62	113.21 ± 0.12
8	59882.4726475694	219.23 ± 0.55	1.60	2.79 ± 0.28	4.47 ± 0.44	5.73	1381.16 ± 6.14	192.61 ± 2.94
			1.60	7.53 ± 0.75	12.05 ± 1.20	17.13	1337.40 ± 7.50	237.15 ± 0.92
9	59883.1097671759	221.16 ± 1.39	6.40	3.95 ± 0.36	25.31 ± 2.32	15.90	1059.68 ± 8.55	217.32 ± 1.40
			6.40	4.18 ± 0.38	26.75 ± 2.45	12.51	1003.38 ± 7.99	120.38 ± 1.10
10	59883.4502390046	219.60 ± 0.68	6.40	2.79 ± 0.26	17.86 ± 1.64	12.75	1301.65 ± 5.71	280.61 ± 5.38
			6.40	2.87 ± 0.26	18.38 ± 1.68	10.73	1200.97 ± 9.44	187.49 ± 1.11
			6.40	4.24 ± 0.39	27.14 ± 2.49	17.26	1120.52 ± 6.76	222.49 ± 0.78
			5.12	5.57 ± 0.51	28.51 ± 2.61	20.53	1094.15 ± 6.03	228.34 ± 1.10
11	59887.3512349537	219.60 ± 2.23	9.60	15.66 ± 1.57	150.34 ± 15.05	84.69	1126.54 ± 4.62	219.55 ± 0.04
			3.84	10.03 ± 1.00	38.53 ± 3.86	35.02	1008.34 ± 4.62	228.68 ± 0.45
			2.56	14.88 ± 1.49	38.08 ± 3.81	37.65	974.84 ± 4.62	180.38 ± 0.39
			3.84	6.78 ± 0.68	26.04 ± 2.61	19.09	966.87 ± 4.91	148.70 ± 1.85
			5.76	10.29 ± 1.03	59.28 ± 5.93	27.37	946.64 ± 4.62	88.50 ± 0.20
12	59887.4423248843	219.86 ± 1.35	2.88	11.63 ± 1.16	33.48 ± 3.35	34.26	1153.26 ± 4.62	217.24 ± 0.09
			6.08	27.24 ± 2.73	165.64 ± 16.58	120.94	1114.70 ± 4.62	233.57 ± 0.01
			5.12	12.46 ± 1.25	63.81 ± 6.39	43.26	967.08 ± 4.62	169.55 ± 0.04
13	59889.1244077662	220.03 ± 0.98	4.48	5.92 ± 0.60	26.53 ± 2.70	20.98	1469.10 ± 4.64	195.59 ± 0.28
			6.40	4.80 ± 0.49	30.71 ± 3.12	26.32	1355.54 ± 4.66	328.12 ± 0.31
14	59889.3744443403	219.77 ± 1.35	7.68	13.49 ± 1.37	103.60 ± 10.54	46.63	947.01 ± 4.64	108.60 ± 0.76
			6.40	5.17 ± 0.53	33.11 ± 3.37	11.77	929.49 ± 4.66	56.48 ± 6.54
15	59890.3176200116	219.57 ± 1.64	2.56	2.58 ± 0.26	6.60 ± 0.67	7.63	1423.93 ± 12.58	242.58 ± 8.22
			7.68	16.86 ± 1.70	129.51 ± 13.06	88.89	1409.52 ± 4.62	256.73 ± 0.03
			5.12	28.24 ± 2.85	144.57 ± 14.58	125.74	1308.04 ± 4.63	274.81 ± 0.02
16	59890.3637615394	220.34 ± 1.43	16.64	4.60 ± 0.46	76.52 ± 7.72	19.92	948.73 ± 4.79	80.03 ± 0.05
17	59891.3109625000	219.49 ± 1.00	3.84	9.85 ± 1.05	37.82 ± 4.01	30.63	978.96 ± 4.82	161.54 ± 0.51
			7.04	16.30 ± 1.73	114.76 ± 12.18	55.80	950.16 ± 4.62	106.73 ± 0.06
			1.92	20.17 ± 2.14	38.72 ± 4.11	33.33	944.70 ± 4.65	91.18 ± 0.27
			3.84	38.79 ± 4.12	148.96 ± 15.81	94.28	939.47 ± 4.62	98.62 ± 0.02
			3.84	11.40 ± 1.21	43.79 ± 4.65	25.54	932.68 ± 4.89	83.77 ± 0.43
18	59891.3164585648	219.29 ± 0.61	1.92	7.66 ± 0.81	14.71 ± 1.56	19.17	1043.39 ± 4.62	209.05 ± 0.32
			1.92	9.09 ± 0.96	17.46 ± 1.85	22.55	1038.36 ± 5.53	205.43 ± 0.26
19	59897.0712164352	219.40 ± 1.11	3.20	16.15 ± 1.61	51.69 ± 5.16	40.72	971.51 ± 2.37	144.12 ± 1.01
			4.48	55.00 ± 5.49	246.42 ± 24.58	146.33	955.11 ± 2.31	114.66 ± 0.05
			5.12	24.72 ± 2.47	126.58 ± 12.62	63.69	949.56 ± 2.31	94.08 ± 0.22
			3.84	17.51 ± 1.75	67.22 ± 6.70	37.72	940.87 ± 2.32	87.74 ± 0.49
20	59898.4399226852	219.91 ± 1.65	4.16	2.48 ± 0.25	10.32 ± 1.03	9.12	1218.58 ± 4.79	233.42 ± 10.08
			5.44	10.64 ± 1.07	57.86 ± 5.80	47.43	1151.51 ± 4.77	262.89 ± 0.23
21	59900.1470432060	220.03 ± 1.45	2.56	9.37 ± 0.93	24.00 ± 2.38	24.36	1059.62 ± 4.17	194.06 ± 1.14
			2.56	22.82 ± 2.26	58.42 ± 5.79	58.10	1056.02 ± 2.32	186.19 ± 0.12
			3.84	30.42 ± 3.01	116.82 ± 11.58	94.34	1030.33 ± 2.31	184.12 ± 0.03
			14.08	28.78 ± 2.85	405.15 ± 40.15	147.22	959.33 ± 2.31	136.69 ± 0.00
22	59900.2719472685	220.00 ± 1.47	5.76	13.64 ± 1.35	78.57 ± 7.79	48.58	963.68 ± 4.63	161.91 ± 0.01
23	59901.4354073148	219.66 ± 1.76	10.24	6.69 ± 0.69	68.46 ± 7.09	49.16	1262.87 ± 4.62	354.94 ± 1.52
			6.40	4.11 ± 0.43	26.28 ± 2.72	18.64	1169.06 ± 4.68	216.43 ± 7.03
			8.32	15.62 ± 1.62	129.93 ± 13.46	80.24	1108.69 ± 4.62	213.32 ± 0.27
			5.76	16.99 ± 1.76	97.86 ± 10.14	52.06	1040.13 ± 7.50	109.59 ± 11.58

Table 2 – *continued*

Index	MJD (d)	DM ($pc\,cm^{-3}$)	Width (ms)	Flux (Jy)	Fluence (Jy-ms)	S/N	Centre frequency (MHz)	Bandwidth (MHz)
24	59903.1278839120	224.94 ± 1.76	5.76	5.13 ± 0.51	29.53 ± 2.93	22.38	1091.56 ± 4.64	242.03 ± 1.30
			4.48	11.86 ± 1.18	53.15 ± 5.28	41.54	1039.08 ± 4.77	200.17 ± 0.29
			4.16	11.31 ± 1.12	47.07 ± 4.68	34.67	983.03 ± 4.62	165.10 ± 0.21
25	59903.2531478009	223.24 ± 1.62	3.20	23.33 ± 2.32	74.64 ± 7.42	86.56	1240.18 ± 4.62	314.81 ± 0.12
			4.48	96.10 ± 9.55	430.55 ± 42.77	407.73	1274.37 ± 4.62	293.91 ± 0.00
			2.88	97.12 ± 9.65	279.71 ± 27.79	329.37	1211.68 ± 4.62	292.13 ± 0.00
			3.52	44.98 ± 4.47	158.33 ± 15.73	155.80	1187.19 ± 4.62	249.33 ± 0.02
			1.92	20.92 ± 2.08	40.17 ± 3.99	49.47	1116.64 ± 4.64	213.09 ± 0.22
			4.48	32.35 ± 3.21	144.93 ± 14.40	127.18	1080.22 ± 4.62	252.39 ± 0.02
26	59904.2669536921	219.46 ± 1.15	10.24	17.17 ± 1.71	175.87 ± 17.48	108.96	1413.36 ± 4.62	287.34 ± 0.34
			8.96	41.23 ± 4.10	369.43 ± 36.71	253.34	1337.74 ± 4.62	308.05 ± 0.08
			6.40	9.60 ± 0.95	61.44 ± 6.11	47.50	1229.29 ± 4.63	279.59 ± 2.61
			6.40	2.82 ± 0.28	18.05 ± 1.79	11.79	1160.55 ± 4.84	199.84 ± 38.37
27	59907.2594524074	219.77 ± 0.43	3.84	2.21 ± 0.21	8.48 ± 0.82	6.39	1067.12 ± 9.71	168.12 ± 1.44
28	59912.2962470023	219.83 ± 1.76	3.20	12.44 ± 1.26	39.82 ± 4.03	22.08	925.77 ± 4.64	69.26 ± 0.02
			3.84	13.22 ± 1.34	50.77 ± 5.14	24.26	920.02 ± 4.63	61.70 ± 0.01
29	59914.2529407407	220.31 ± 2.56	6.40	30.83 ± 3.15	197.31 ± 20.15	93.40	936.72 ± 4.62	99.31 ± 0.06
			5.76	3.53 ± 0.36	20.31 ± 2.07	7.49	940.03 ± 4.64	54.19 ± 7.29
30	59915.2896052546	219.60 ± 1.11	9.60	2.44 ± 0.25	23.47 ± 2.39	13.22	1013.09 ± 7.50	211.43 ± 4.31
			7.04	15.45 ± 1.58	108.78 ± 11.09	61.20	951.36 ± 4.62	154.67 ± 0.15
			4.48	5.26 ± 0.54	23.58 ± 2.40	16.52	954.24 ± 4.67	152.58 ± 2.56
			8.32	2.92 ± 0.30	24.30 ± 2.48	8.34	956.78 ± 6.55	68.03 ± 1.25
31	59916.3118642361	220.11 ± 1.20	6.40	5.25 ± 0.52	33.59 ± 3.32	22.81	1162.06 ± 5.44	218.62 ± 0.20
32	59920.2334853009	219.83 ± 1.25	4.48	12.14 ± 0.79	54.38 ± 3.55	25.46	1080.98 ± 4.71	166.28 ± 0.11
33	59930.1239017014	219.55 ± 0.98	3.20	7.75 ± 0.79	24.81 ± 2.52	20.48	970.46 ± 4.74	152.34 ± 1.21
			3.20	8.53 ± 0.87	27.31 ± 2.78	17.46	968.14 ± 4.67	91.45 ± 1.13
			1.28	5.64 ± 0.57	7.21 ± 0.73	4.47	986.71 ± 4.89	34.28 ± 1.41
34	59931.2705442477	219.77 ± 1.43	5.12	4.27 ± 0.43	21.87 ± 2.22	15.82	999.10 ± 4.73	188.25 ± 1.60
			2.56	3.74 ± 0.38	9.58 ± 0.97	5.15	966.17 ± 5.40	51.96 ± 2.06
			2.56	21.32 ± 2.16	54.58 ± 5.53	35.14	936.37 ± 4.91	74.58 ± 0.11
35	59933.1711922801	219.86 ± 1.12	3.20	2.07 ± 0.22	6.62 ± 0.69	7.28	1041.30 ± 9.47	254.05 ± 6.32
			5.12	24.94 ± 2.62	127.72 ± 13.40	90.72	979.10 ± 4.62	169.45 ± 0.03
			3.20	58.65 ± 6.15	187.69 ± 19.69	162.29	968.05 ± 4.62	156.93 ± 0.01
			3.20	84.50 ± 8.86	270.39 ± 28.37	234.56	963.53 ± 4.62	157.97 ± 0.01
			3.20	33.11 ± 3.47	105.94 ± 11.11	79.37	948.45 ± 4.62	117.81 ± 0.03
			4.48	26.32 ± 2.76	117.92 ± 12.37	68.89	940.82 ± 4.62	100.29 ± 0.05
			8.00	25.42 ± 2.67	203.35 ± 21.33	85.77	935.08 ± 4.62	93.35 ± 0.01

we crop the array to ± 100 bins (6.4 ms) on this range. Finally, the files are written out as dynamic spectra with accompanying metadata containing information about the time axis, frequency axis, dispersion measure, and various units.

We open these dedispersed and cropped files with FRBGUI. For each file, we define a DM grid covering the original SPANDAK DM ± 0.5 $pc\,cm^{-3}$, sampled at 0.01 $pc\,cm^{-3}$ intervals. If the average DM of the whole sample would fall outside of this grid, we extend it by another ± 0.5 $pc\,cm^{-3}$ in the relevant direction. We then optionally perform a series of tasks to improve the SNR of the burst:

(i) *Subtract a background sample from the entire dynamic spectrum*: This background sample is usually selected to be the first few milliseconds of the file before the burst begins. This helps remove narrowband RFI.

(ii) *Add a frequency mask range*: For bursts that do not cover the entire bandwidth (most of them, as per Fig. 1), we can mask up to hundreds of MHz of bandpass where there is no FRB signal in order to improve the SNR.

(iii) *Remove remaining RFI*: For bursts with significant RFI, we implemented built-in RFI-masking with a spectral kurtosis – Savitzky–Golay filter (with a polynomial order of $\sigma = 3$ and a a window-size of 15 samples), which improved the SNR. For less affected bursts, however, this removed the brightest parts of the true FRB signal and was not used.

(iv) *Downsample in time and frequency:* By downsampling, or frequency averaging and time integrating the dynamic spectrum, we can improve the SNR – this is especially necessary for faint FRBs and was already part of SPANDAK's routine for finding these fainter FRBs. We select time and frequency downsampling factors that are evenly divisible into the length of the array axes, while still endeavoring to keep enough resolution to be confident of e.g. drift rates.

We then manually demarcate burst splitting with FRBGUI's interactive interface. Given that FRBs have been shown to have sub-bursts and structure on the order of microseconds (Nimmo et al. 2022), and that we are downsampling to increase SNR, there are likely fine-structure details that we cannot resolve in our data set. Nevertheless, we do delineate the sub-bursts that are visible given our resolution, and find FRBs with up to seven distinct components in our 35 burst data set.

Finally, we use a non-linear least-squares algorithm[4] to perform a 6-parameter 2D Gaussian fit to the 2D auto-correlation of the dynamic spectrum for the entire array, and then for the limited sub-arrays delineated in time by each sub-burst start and stop defined previously. Fitting to the auto-correlation increases the SNR and mitigates the effect of e.g. scintillation and RFI in the parameter measurements (see Chamma et al. 2023 for more details about this operation). For each DM in the grid, the fitter returns the bandwidth, duration, and sub-burst slope for each of the sub-bursts, as well as the bandwidth, duration, and drift rate (in MHz ms^{-1}) of the overall burst, with their associated errors. In some cases, the fitter does not converge on the correct parameters for the burst. We visually reviewed each fit (for every DM-sub-burst combination) in the FRBGUI interface and, where necessary, implemented a refit by manually inputting an initial guess based on the correct preceding fits.

The centre frequency, duration, and bandwidth information for each sub-burst are shown in Table 2. Reported uncertainties in the duration are equal to the time bin size after scrunching in the dynamic spectrum used for the spectral property fitting.

4 DATA ANALYSIS

4.1 Spectrotemporal analysis

Using the FRB and sub-burst characteristics extracted in Section 3, we can investigate population-scale features of our data set. The centre frequencies, durations, and bandwidths for all 101 sub-bursts in the set are displayed in Fig. 3.

For all linear fits in Sections 4.1.2–4.1.5, we use the following methodology. In most cases, we have an independent variable x, a dependent variable y, and heteroscedastic errors in each variable $x_{\rm err}$ and $y_{\rm err}$. We account for this heteroscedasticity with a bootstrapping technique. We employ an ordinary least-squares (OLS) fitting method that incorporates robust covariance estimators (specifically, the HC1 estimator from MacKinnon & White 1985). In each of 10 000 bootstrapped trials, we draw each value of x or y from a normal distribution with a width of $x_{\rm err}$ or $y_{\rm err}$, respectively, and then use the OLS fitting method to get a value for the slope and its associated R^2 value (the square of the Pearson correlation coefficient, to quantify how much variance in the dependent variable is explained by the independent variable).

For each fit, we report (a) the mean of the 10 000 slopes from the trials above (b) the mean of the 10 000 standard errors of the slope, and (c) the mean of the R^2 values of the 10 000 trials. We calculate the significance of these correlations by running an additional 10 000 trials where we permute the data, i.e. randomly shuffle the y values and then re-assign them to the x values. The p-value is then the percentage of permuted outcomes that meet or exceed the absolute value of the mean R^2 described above. Here, we use $p < 0.05$ as our threshold for statistical significance.

4.1.1 *Burst energy*

To compare our sample with the energy distribution of 128 bursts seen by the Green Bank Telescope (Feng et al. 2023), we can convert the fluences from Section 3.2 into isotropic equivalent sub-burst energies, using the redshift and luminosity distance from Planck Collaboration XIII (2016); Ravi et al. (2022), which assumes Planck 2016 cosmology. We find a median sub-burst energy for our sample

[4]Via `scipy.optimize.curve_fit`

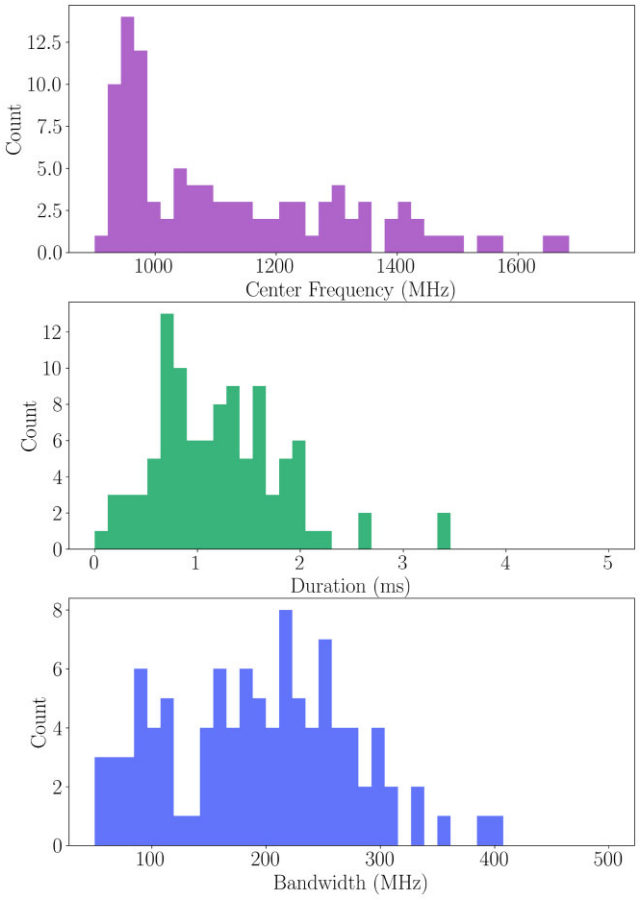

Figure 3. The distributions of centre frequency in MHz, duration in ms, and bandwidths in MHz for each of the 101 sub-bursts in the data set. We see the majority of FRBs reside at the lower end of the bandpass, have <2 ms durations and show bandwidths of a few 100 MHz.

of 1×10^{39} erg, approximately two orders-of-magnitude greater than the median from Feng et al. (2023), although approximately on-par with their brightest bursts. This is consistent with the lower sensitivity of the ATA. The brightest sub-burst in our sample, from #25, has an energy of 1.8×10^{40} erg; the brightest burst, combining all subbursts (also #25), has an isotropic energy of 5×10^{40} erg.

4.1.2 *Centre frequency versus bandwidth*

To test the correlation between the centre frequency of a sub-burst and its bandwidth, we first remove any FRB from the set whose sub-bursts significantly intersect the edge of the band by visual inspection of the de-dispersed dynamic spectra. This results in a set of 55 sub-bursts for which we evaluate a linear fit. We find a positive, linear correlation between centre frequency and bandwidth with a slope of 0.28 ± 0.04, as shown in Fig. 4. The R^2 for the fit between the centre frequency and bandwidth is 0.533 and the p-value is $<10^{-4}$.

This slope is consistent within a factor of two of the slope of 0.14 ± 0.004 found by Chamma et al. (2023) for FRB 20121102A, although different sources would not necessarily be expected to have the same slope. The centre frequency and bandwidth relationship described here also appears consistent with the 1000-burst data set from Zhang et al. (2023).

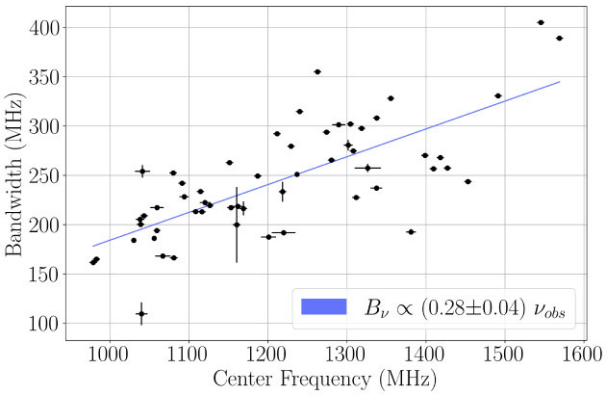

Figure 4. Centre frequency in MHz versus bandwidth in MHz for 55 sub-bursts from FRB 20220912A (black) and their best-fitting tingline (blue). 1-σ fit errors derived by FRBGUI are shown in both centre frequency and bandwidth for the points used in the linear fit, which were accounted for during the bootstrapping. We confirm the expected positive linear relationship between these two properties.

4.1.3 Centre frequency and bandwidth versus time

A unique feature of our data set was the relatively steady rate of data acquisition over the two months of the campaign; this can be seen in the smooth slope of the cumulative observing time in Fig. 2. This allows us to interrogate changes in the properties of the 101 sub-bursts from FRB 20220912A over time. We see a decrease in both the centre frequency and bandwidth over the course of the campaign (Fig. 5). The centre frequency decreases at a rate of 6.21 ± 0.76 MHz d^{-1}, with a corresponding R^2 of 0.311 and a p-value of $<10^4$. This trend is echoed by the bandwidth, which decreases 2.08 ± 0.38 MHz d^{-1}, with a corresponding R^2 of 0.191 and a p-value of $<10^4$, due to their inherent relationship shown in Fig. 4. There were no similarly obvious changes in flux, duration, or DM over the campaign.

Other repeaters have been observed to have varying activity levels at different frequency ranges. For example, FRB 20180916B shows activity in the 1000 MHz range 3 d before activity peaks in the 100 MHz range (Pleunis et al. 2021a). Pearlman et al. (2020) also find that apparent FRB activity is strongly affected by which frequencies are being recorded, with FRB 20180916B again showing this behaviour particularly strongly. However, this marks the first trend in frequency over time for a so-far non-periodic (as per Zhang et al. 2023) repeating FRB.

The residuals from the linear fit of central frequency over time in Fig. 5 do merit discussion. We find some remaining structure in the residuals, where the best-fitting model underestimates the centre frequency at the beginning of the campaign and overestimates the centre frequency at MJD 59890. Without an underlying model to compare to, we do not attempt to fit a more complex function to the data, but do note this behaviour as something to be investigated in future studies. In addition, the residuals in this linear fit are not homoskedastic: the scatter around the best-fitting line decreases over the campaign. These heteroskedastic errors should raise some questions about the extension of this trend past the bottom of our bandpass. Specifically, it seems possible that there is a several hundred MHz wide, downward drifting 'activity window' in frequency, that drifts out of our bandpass over the campaign. This leads to the apparent shrinking of the scatter at the end of the linear fit, and implies that the actual slope in the central frequency may be steeper than 6.2 MHz d^{-1}.

4.1.4 Centre frequency versus drift rate

Other repeaters have shown a correlation between centre frequency and drift rate, the linear decrease in sub-burst centre frequency over time. We use the values derived by FRBGUI in Section 3.3 to assess whether we see this same correlation in the FRB 20220912A data. It should be noted that no FRBs in our sample show upward-drifting bursts (e.g. Kumar et al. 2022).

To construct a subsample with reliable drift rate measurements, we must first remove all of the single-component FRBs, which do not have a defined drift rate. In addition, the Auto-Correlation Function (ACF) method for sub-burst centre frequency determination will underestimate the centre frequencies of components that intersect the top edge of the bandpass, and correspondingly overestimate the

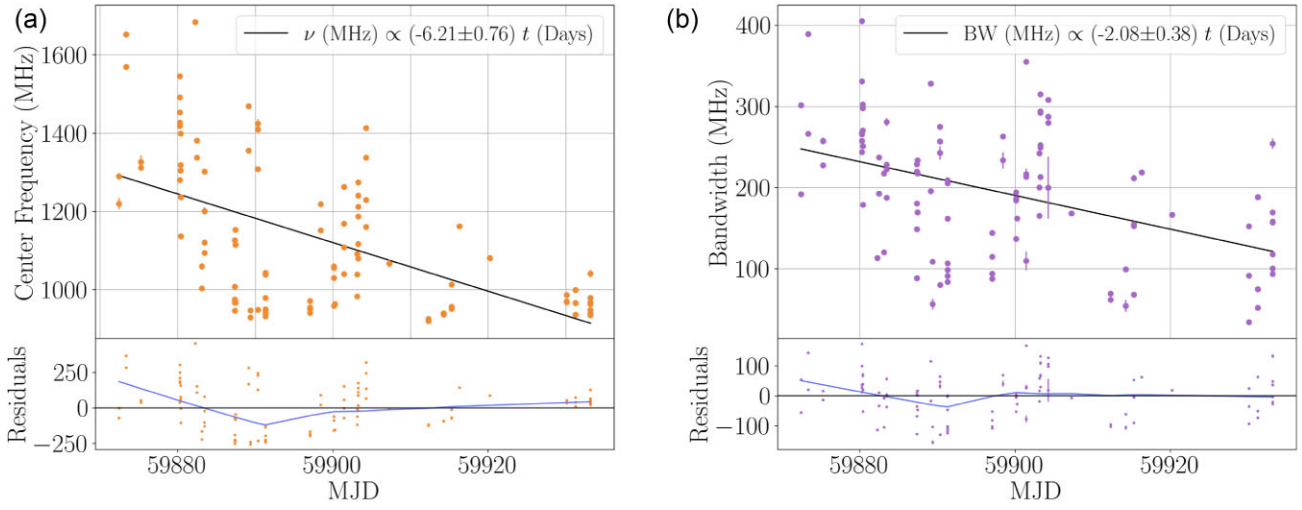

Figure 5. Two FRB 20220912A data set parameters – centre frequency and bandwidth – plotted over time, in MJD, from the beginning of the campaign to the end of the campaign (a time period of approximately 60 d). Panel (a) indicates that the central frequency of the FRB decreases through the campaign (with residuals from the fit and a LOWESS non-parametric guideline shown below in blue). Panel (b) shows the same decrease over time for bandwidth, which is understandable given the relationship between bandwidth and centre frequency shown in Fig. 4.

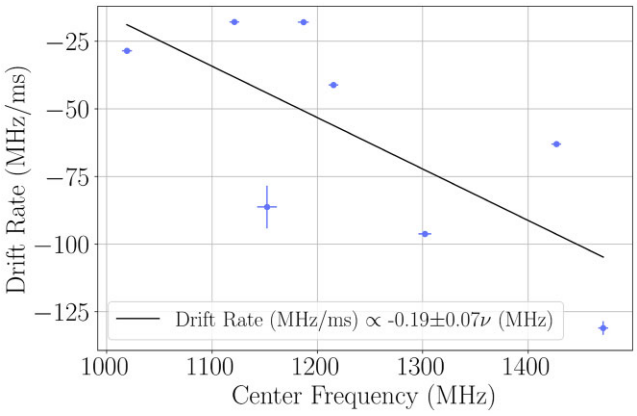

Figure 6. Drift rates in MHz ms^{-1} plotted against frequency in MHz for eight FRBs from FRB 20220912A that (a) had more than 1 subcomponent (b) did not intersect either edge of the bandpass and (c) had subcomponents of similar-enough SNRs to allow for a correct drift rate fit from the 2D ACF of the dynamic spectrum. Visually, there is a downward trend (increasing magnitude of drift) with increasing frequency and we show the best-fitting line from a linear fit (black), but we do not find that this trend is significant.

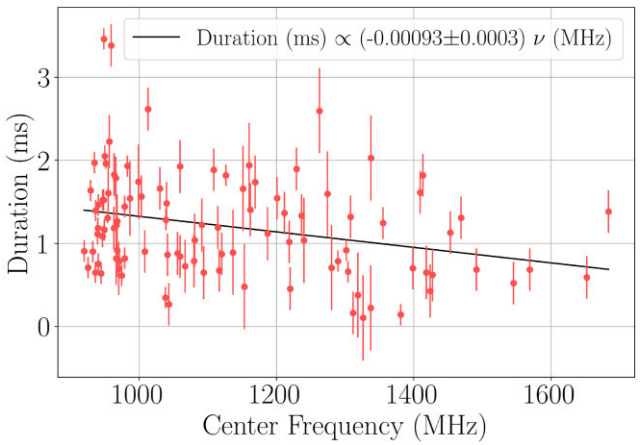

Figure 7. Duration in ms plotted against frequency in MHz for our full sample of 101 sub-bursts from FRB 20220912A. Note the slight decrease in duration over the bandpass.

centre frequencies of components that intersect the bottom edge of the bandpass. Both effects lead to an underestimation of the drift rate: therefore, we remove any FRBs that intersect the edges of the bandpass, bringing the subsample to 11 FRBs. Finally, we wish to remove any FRB where the ACF measured the sub-burst slope of the brightest component instead of the drift rate across multiple components, which can occur in FRBs with large SNR variation across sub-bursts. This effect is visible in the 2D-ACFs, and can be confirmed as an anomalously high drift rate that is consistent with a single sub-burst's slope. For this reason, we additionally remove FRBs #3, #6, and #18.

We plot the drift rates for the eight remaining FRBs (#1, #4, #8, #10, #20, #23, #24, and #25) against their centre frequencies in Fig. 6 and do not find a statistically significant correlation. We used an $N = 10^5$ trial bootstrap for this correlation, due to p-values that were near the threshold. The bootstrapping OLS routine finds a slope of -0.189 ± 0.07 MHz ms^{-1} MHz^{-1} and an R^2 of 0.502, but the p-value of 0.052 is not significant. This is consistent with the data, considering the small-number statistics resulting from only eight FRBs in the fit.

Other repeating FRBs demonstrate a trend of steeper drift rates with frequency. For FRB 20180916B, compilations of studies across wide bandwidths have shown a drift rate change of -0.02 to -0.03 MHz ms^{-1}MHz^{-1} with frequency (Pastor-Marazuela et al. 2021; Sand et al. 2022). Meanwhile, for FRB 20180301A (at frequencies an order-of-magnitude higher), Kumar et al. (2023) find a drift rate change of -0.14 MHz ms^{-1} MHz^{-1} with frequency, over approximately the same frequency range as this work. Using MeerKAT, Platts et al. (2021) find a similar drift rate change with frequency, -0.147 ± 0.014 MHz ms $^{-1}$ MHz^{-1}, for FRB 121102. It should be noted that a quadratic fit is favoured when data covers a larger range of frequencies (Wang et al. 2022; Chamma et al. 2023). Given that our measurement was not significant, we cannot add to this population of results with FRB 20220912A in this work; regardless, the consistency of the sign and general relationship of frequency and drift rate over this population of repeaters hints at a persistent feature in at least a subclass of FRBs that must be explained by any proposed emission mechanism.

Sub-burst slope and drift rate can follow similar relationships (e.g. Rajabi et al. 2020; Chamma et al. 2023). However, we see no correlation between sub-burst slope and duration, or sub-burst slope and centre frequency, in this data set. Given the scatter in the measurements and the lack of bursts at other bands to constrain model fits, this is not unexpected.

4.1.5 Centre frequency versus temporal duration

It has been noted that higher frequency sub-bursts seem to have shorter temporal durations, which is only observable across GHz of bandwidth (e.g. Platts et al. 2021). Gajjar et al. (2018) notes that the widths are considerably narrower (about an order of magnitude) at 8 GHz compared to 1 GHz for FRB 121102, but that the effect does not seem consistent with broadening due to scattering from turbulent plasma along the line-of-sight. Here, we do observe a slight downward trend in duration with increasing frequency, as shown in Fig. 7. The associated linear fit has a slope of $(-\ 9.3 \pm 3.3) \times 10^{-4}$ MHz ms^{-1}, an R^2 value of 0.067 (indicating wide scatter over the $\sim$700 MHz available in these observations), and a p-value of 0.0098. Given the low correlation, this result should be taken only as an indication of consistency with the previously observed trend of shorter durations at higher central frequencies. Given the channel width and the FRB DM, the expected smearing due to dispersion at the bottom of the ATA band is $\sim$0.9 ms.

4.1.6 Scattering

We do not observe any significant scattering behaviour in the waterfall plots in Fig. 1, though we cannot constrain scattering time-scales less than several hundred μs at these frequencies, due to our sampling time of 64 μs. This is consistent with the nominal scattering value of $\leq$15 ms at 400 MHz for this source as reported by Bhusare et al. (2022), which would imply, given a Kolmogorov scaling with $\alpha = 4.4$, an expected scattering time-scale of $\leq$60 μs.

4.2 Repeating rate function and all-sky rate

We show the cumulative repeating rate function R ($>F$) for FRB 20220912A in Fig. 8, where F is the fluence of each FRB (which may contain multiple sub-bursts). We fit the observed

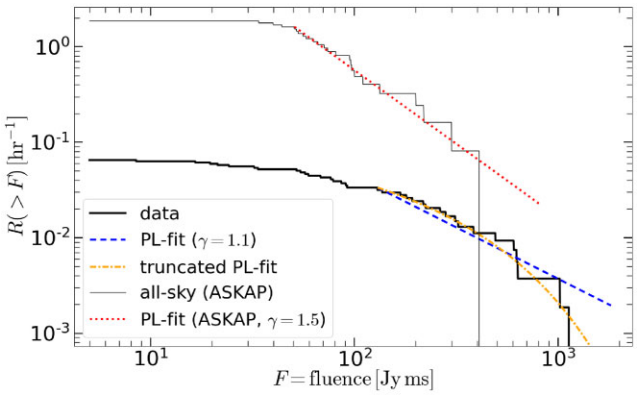

Figure 8. Fluence distributions of the ATA sample of bursts from FRB 20220912A (thick black line) and the Australia SKA Pathfinder Telescope (ASKAP) Fly's Eye sample (thin black line). The vertical axis shows the cumulative rate, as computed by the raw number of detections divided by the total on-source time. The total exposure of the ASKAP Fly's Eye survey is 5.1×10^5 deg^2 h (Shannon et al. 2018), which is converted into an all-sky equivalent exposure time of 12.4 h – the thin black line shows the all-sky rate as inferred from the ASKAP sample. The flattening of the distributions at the low fluence end ($\lesssim 100$ Jy ms for the ATA sample and $\lesssim 50$ Jy ms for the ASKAP sample) is likely due to incompleteness of the surveys. The steepening at the high fluence end is due to insufficient exposure times. The blue dashed and orange dash–dotted lines show the best-fitting power-law and truncated power-law models to the ATA data, respectively. The red dotted line shows the best-fitting power-law model for the ASKAP data.

fluence distribution with a power-law function using the `powerlaw` package provided by Alstott, Bullmore & Plenz (2014) based on Clauset, Shalizi & Newman (2009). The package uses the maximum likelihood method to optimize the power-law slope $\gamma \equiv -\mathrm{d}\ln[R(>F)]/\mathrm{d}\ln F$ and further uses the Kologorov–Smirnov test to optimize the minimum fluence $F_{\rm min}$ above which a power-law provides the best description (see Clauset, Shalizi & Newman 2009, for the method descriptions).

When restricting the minimum fluence to be in the range from 40 to 150 Jy ms (roughly corresponding to a minimum SNR between ∼40 and ∼150 for burst duration of ∼1 ms), we find the optimized minimum fluence to be $F_{\rm min} \simeq 130$ Jy ms. We also find the best power-law above this minimum fluence to be

$$R(>F) = 3.3 \times 10^{-2}\,\mathrm{h}^{-1}\,(F/F_{\rm min})^{\gamma},\ \gamma = 1.08, \quad (5)$$

and the standard deviation of the power-law slope is $\sigma = 0.25$. The slope is not well constrained by the current small sample but it is consistent with the power-law slope of the FRB luminosity (or energy) function (e.g. Luo et al. 2018; Lu & Piro 2019; James et al. 2022; Shin et al. 2023). We also tried fitting the ATA sample by an exponentially truncated power-law described by $R(>F) \propto F^{\gamma}\exp(-F/F_{\rm max})$, and the best fitting result is $\gamma \simeq 0.0$ and $F_{\rm max} \simeq 570$ Jy ms. Although the likelihood ratio test shows that a truncated power-law fit is preferred with a p-value of 0.06 – meaning that there is a 6 per cent chance that the improvement in the likelihood is due to random fluctuations, the truncated power-law model has an additional free parameter and hence a truncation is not required by the current data.

We then compared the repeating rate function for FRB 20220912A with the cumulative all-sky rate function at high fluences, which is provided by the ASKAP Fly's Eye survey (Shannon et al. 2018). Using the same method as outlined above, we find that the all-sky rate function can be described by the following best-fitting power-law function above an optimized minimum fluence of $F_{\rm min} = 50.6$ Jy ms,

$$R_{\rm as}(>F) = 1.6\,\mathrm{h}^{-1}\,(F/F_{\rm min})^{\gamma_{\rm as}},\ \gamma_{\rm as} = 1.54, \quad (6)$$

and the standard deviation of the power-law slope is $\sigma_{\rm as} = 0.34$. Despite that $\gamma_{\rm as}$ is statistically weakly constrained, we do theoretically expect the fluence distribution to be close to the Euclidean value of $\gamma = 1.5$ because the ASKAP bursts are from the local Universe and the entire FRB population has a maximum specific energy (see e.g. Macquart & Ekers 2018; Lu & Piro 2019; Shin et al. 2023).

It should be noted that the specific energy of the brightest burst ($F = 1128$ Jy ms) detected in our sample is

$$E \simeq \frac{F \times 4\pi D_{\rm L}^2(z)}{(1+z)^2} \simeq 1.5 \times 10^{32}\,\mathrm{erg\,Hz^{-1}}, \quad (7)$$

where we have used the Planck Collaboration XIII (2016) cosmological parameters for the luminosity distance $D_{\rm L}$ and a source redshift of $z = 0.077$ provided by Ravi et al. (2022). This burst is among the most intrinsically bright ones observed to-date (e.g. Ryder et al. 2022; Shin et al. 2023). As can be seen in Fig. 8, the repeating rate function of FRB 20220912A must have a cut-off at fluence $F_{\rm max} \lesssim 10^4$ Jy ms for this source to be consistent with the all-sky fluence distribution extrapolated from the ASKAP measurement assuming $\gamma_{\rm as} = 1.5$ (and additionally assuming that the repetition rate of this source is constant). Such a cut-off is also consistent with the inferred maximum specific energy $E_{\rm max} \sim 10^{32}$ to 10^{33} erg Hz^{-1} in the FRB luminosity/energy function (Shin et al. 2023). Further long-term monitoring of FRB 20220912A is needed to test if the repeating rate function indeed has a cut-off.

On the other hand, we also see from Fig. 8 that FRB 20220912A contributes at least a few per cent of the all-sky rate above fluence of ∼ 100 Jy ms. Although prolific repeaters like FRB 20220912A and FRB 20121102A represent a minority of all FRB sources, they contribute a significant fraction of the all-sky rate. On the other hand, many of the > 100 Jy ms sources detected by the ASKAP Fly's Eye did not show repetitions even with sensitive follow-up observations. This means that the brightest FRBs in the sky are contributed by the most active repeaters as well as by the less active ones. This further restricts the maximum fluence of FRB 20220912A to be likely significantly less than 10^4 Jy ms.

4.3 Characteristic time-scales and sub-burst periodicity

Given that so many of our FRBs are multi-component (29/35), we investigate whether or not the sub-bursts show any consistent interpulse spacings. In particular, FRB #10 shows four sub-bursts that are bright and appear evenly spaced, hinting at sub-burst periodicity. For both a general characteristic time-scale analysis and a periodicity analysis, we begin with the NUMPY arrays produced in Section 3.3, and average over the frequency axis to get a timeseries profile. We then median-subtract and apply a 5th-degree polynomial Savitzky–Golay filter with a window-size of 21 samples (Savitzky & Golay 1964). The smoothing filter is applied to make peak-finding possible in Section 4.3.1, but does attenuate potential short-period behaviour (≲0.13 ms) in the FRB profile.

4.3.1 Characteristic time-scales

To characterize significant time-scales in each FRB, we calculate the ACF of the smoothed FRB profile with SCIPY. This allows us to be more sensitive to non-sinusoidal signals with fewer repetitions in short timeseries than a power spectrum (e.g. a Leahy-normalized

power spectrum, see CHIME/FRB Collaboration 2022) while still performing a similar function.

We then find the tallest local maximum in the ACF with a required minimum peak width of $w_{\rm ACF} > 2$ bins (to avoid single-bin noise fluctuations). This corresponds to the lag time $p_{\rm ACF}$ which contains the most power in the ACF – if the FRB is generating the peak in the ACF, this is likely representative of the delay in sub-bursts for a two-component FRB. At this stage, 2 of the 35 FRBs were removed from the sample due to not having any peaks in their ACFs.

RFI is often periodic and could create a false-positive periodicity in the ACFs from the previous step. Therefore, we perform a bootstrap resampling noise-permutation test as a crude filter for ACF peaks that are not coming from the FRB signal itself. Each file contains 100 channels of noise before and after the FRB, which constitutes 25 per cent or more of each file (depending on the variable FRB duration; mean = 42 per cent). For each FRB, we perform 1000 trials where the noise arrays before and after the FRB signal are randomly shuffled, and then perform the median-removal, smoothing, ACF, and peak-finding steps as for the original FRB profile. If the mean of the set of 1000 noise-scrambled ACF peaks still falls within 10 per cent of the original, with a standard deviation that is less than the width of the peak $w_{\rm ACF}$ from the original ACF, we treat this as a spacing that is inherent to the FRB itself. We find that 21 of the remaining 33 FRBs pass this filter. Those 21 ACF peak spacings were then visually checked against the timeseries profiles, to ensure that the above methodology returned results that were consistent with the visual appearance of the FRB. It should be noted that peaks in an ACF can be difficult to interpret or assign significances to; for example, for FRBs with complex quasi-periodic structure, this could be representative of the distance between the two brightest sub-bursts, or an indication of evenly spaced components.

The median and median absolute deviation of the distribution of ACF-derived time-scales is 5.82 ± 1.16 ms. This implies that, while individual bursts may have preferred periods or spacings, we do not see a sharp mode or otherwise tightly clustered distribution providing evidence of a shared, strict periodicity between sub-bursts across the sample, which corroborates the report of no 1 ms–1000 s periodicity from Zhang et al. (2023).

In the future, this sort of technique would be improved by fitting for the FRB shape, subtracting it from the data, and then fully permuting the remaining profile, instead of the 'bookend' noise-permutation method described above.

4.3.2 *Sub-burst periodicity*

As noted by Petroff, Hessels & Lorimer (2022), strict periodicity even within a single sub-burst (as in CHIME/FRB Collaboration 2022) supports a magnetospheric origin of FRB emission, given that it is difficult to produce with an external shock model. Visually, FRB # 10 is a candidate for this kind of strict periodicity. To assess the statistical significance of the periodicity in this particular burst, we employ methodology similar to CHIME/FRB Collaboration (2022), as follows.

We first check for a peak in the squared Fourier transform, which we find at 6.4 ms (the ACF peak for this FRB was at 5.7 ms). To find actual times-of-arrival (ToAs) of each of the four subbursts, we perform a least-squares fit of a function containing four Gaussians (each with independent amplitude, width, and central time) and a constant vertical offset. Using the results of that fit, we extract the central times as the ToAs; we then re-fit while enforcing a constant spacing between peaks, letting only period and start time of the first subburst vary while fixing the amplitudes, widths, and offset to the best-fitting values from the previous fit. The resulting best-fitting period is 6.1 ms.

To assess the significance of this result, we calculate the $\hat{L}[n]$ statistic from CHIME/FRB Collaboration (2022), a metric of how well the ToAs approximate the linear relationship expected for arrival time versus integer multiples of the best-fitting period (where larger scores equal better approximation). Using the ToAs obtained in the first 4-Gaussian fit and a 6.1 ms period, we find $\hat{L}[n]_{FRB10} = 3.459$. Then, we simulate 10 000 arrays of four ToAs each, with the following conditions:

(i) Average spacings $\bar{d}$ that would enforce all four pulses falling within the length of the timeseries
(ii) An 'exclusion factor' (minimum spacing factor) of $\chi = 0.2$
(iii) ToAs drawn from a uniform probability distribution between $\chi\bar{d} \leq d \leq (2-\chi)\bar{d}$

This creates series of four ToAs that are not drawn from a periodic distribution, but will have a range of scores in $\hat{L}[n]$ which could, in cases, approach periodicity. When we compare $\hat{L}[n]_{\rm FRB10}$ to the distribution of $\hat{L}[n]$ values from the simulations, we find that it is larger than 81 per cent of values in the simulation, giving a generous 'false alarm probability' of 19 per cent. From this result, we cannot reject the null hypothesis of a non-periodic emission mechanism. Note that the first two sub-pulses are particularly low SNR, so their Gaussian-fitted ToAs may be contributing to the lower $\hat{L}[n]$ score.

We also see no obvious periodicity between bursts. However, we note that, because the ATA can only observe the part of the FRB's energy distribution that is above both bimodal peaks seen by Zhang et al. (2023) and Feng et al. (2023), our sampling of periodicity or patterns in wait-time will be incomplete.

5 DISCUSSION AND CONCLUSION

As described in Section 2.3, we detect 35 bursts from the FRB 20220912A in 541 h of observation with the ATA, using the SPANDAK detection pipeline. The FRBs appear throughout the 672 MHz bandpass, biased towards the lower (∼1 GHz) frequency end, with an average sub-burst duration of 1.2 ms and an average sub-burst bandwidth of ∼200 MHz. In Section 3, we used the FRBGUI package, which leverages 2D fits to the ACF of the dynamic spectrum of each bursts, to measure spectrotemporal features from each FRB. In Section 4, we described the following features in our data set:

(i) A median dispersion measure of 219.775 pc cm^{-3} (Section 3.1)
(ii) A median isotropic equivalent burst energy of 1×10^{39} erg (Section 4.1.1)
(iii) A positive, linear correlation between centre frequency and bandwidth (Section 4.1.2)
(iv) A decrease in centre frequency and bandwidth over the two months of the campaign (Section 4.1.3)
(v) A slight decrease in duration with increasing centre frequency (Section 4.1.5)
(vi) No evidence for scattering (Section 4.1.6)
(vii) FRB 20220912A must have a cut-off fluence $F_{\rm max} \lesssim 10^4$ Jy-ms to be consistent with the all-sky fluence distribution (Section 4.2)
(viii) FRB 20220912A significantly contributed to the all-sky FRB rate at a level of a few per cent for fluences $\gtrsim$100 Jy-ms (Section 4.2)
(ix) The majority of bursts in the observed sample were multi-component FRBs, with median component spacings of 5.82 ± 1.16 ms (Section 4.3.1)

(x) No bursts showed statistically significant sub-burst periodicity (Section 4.3.2)

Broadly speaking, there are two classes of FRB models depending on whether the radio bursts are created within the magnetosphere of a neutron star (or black hole) or far from the magnetosphere.

One of the close-in models is coherent curvature emission, where charged particles in macroscopic clumps of longitudinal sizes $\lesssim \lambda$ (the FRB wavelength) radiate coherently when moving along curved magnetic field lines (e.g. Lu & Kumar 2018; Lu, Kumar & Zhang 2020). In this model, the FRB spectrum is set by the spatial distribution of currents in the longitudinal direction. By Fourier transformation, a narrow spectrum of $\Delta\omega/\omega_{\rm centre} \simeq 0.3$ can be produced by a modestly long ($N \sim$ few) chain of current islands.

One class of the far-away models relies on synchrotron maser emission when an ultra-relativistic outflow interacts with strongly magnetized plasma forming a quasi-perpendicular shock (Hoshino & Arons 1991; Metzger, Margalit & Sironi 2019; Plotnikov & Sironi 2019). The synchrotron maser model predicts $\Delta\omega/\omega_{\rm centre} \gtrsim 1$ for two reasons: (1) the ring-like particle distribution function is not infinitely thin in phase space but with a fractional momentum spread of order unity – this allows the rapid growth of modes at a rather broad range of frequencies $\Delta\omega'/\omega'_{\rm centre} \sim 1$ (here, primes $'$ mean in the comoving frame of the shocked plasma) instead of a narrow spectral line (Plotnikov & Sironi 2019; Sironi et al. 2021); (2) the Doppler beaming for viewing angles of $\lesssim 1/\Gamma$ across a quasi-spherical shock front creates a broad spectrum $\Delta\omega/\omega_{\rm centre} \sim 1$ in the observer's frame (Metzger, Margalit & Sironi 2019; Beniamini & Kumar 2020). Previous observations show that many bursts, especially those from repeaters (Pleunis et al. 2021b), have narrow bandwidths $\Delta\omega/\omega_{\rm centre} \ll 1$. For the synchrotron maser model to be viable for these narrow-banded bursts, external propagation effects (e.g. Cordes et al. 2017; Sobacchi et al. 2022) must be playing a role at modulating the spectral intensity across narrow frequency intervals.

While magnetar models are currently favoured, other exotic repeater models do exist. For example, superradiance models rely on a narrowband emitter similar to a molecular maser, and triggered superradiance models invoke FRBs initiated in the system by a more distant coherent emitter such as a pulsar (Dicke 1954; Houde et al. 2019).

The conclusions in the list above do not strongly favour or disfavour any of the described classes of models, but do provide a benchmark against which to compare future observations. For example, it remains to be shown how (and if possible at all) propagation effects in the synchrotron maser model would create a linear correlation between the bandwidth and the central frequency as seen in this work. This same observation, as well as the tentative decrease in duration with centre frequency, is consistent with a narrowband emission process such as that in the superradiance model (Rajabi et al. 2020).

Regardless of the model's location of emission, our results underscore the conclusions found in Feng et al. (2023) and Zhang et al. (2023): low-efficiency models (with efficiencies of order 10^{-4} or lower) for the emission mechanism are not compatible with the immense energy being released and the high activity rate of this FRB source, especially given that our sample consists of bursts with a median energy $\sim$100$\times$ that of the previous literature.

All of the published bursts for this source, our 35 included, are downward-drifting, potentially indicating that downward frequency drift is inherent to the emission mechanism; this is a feature consistent with both close-in and far-away magnetar models.

This work emphasizes the importance of the ATA in FRB science, given its wide bandwidth recording capabilities and potential to engage in unique modes of observation, for example, a 'Fly's Eye' strategy covering up to a 389 deg^2 field-of-view on the sky at 1 GHz (Siemion et al. 2011). As the refurbishment continues, additional FRB-relevant features, such as a fast imaging mode will be re-implemented on the upgraded system (Law & ATA Team 2009). More observations of the source, especially at higher frequencies with instruments like the ATA, will help to differentiate between the various classes of FRB progenitor models.

ACKNOWLEDGEMENTS

The Allen Telescope Array (ATA) refurbishment programme and its ongoing operations have received substantial support from Franklin Antonio. Additional contributions from Frank Levinson, Greg Papadopoulos, the Breakthrough Listen Initiative, and other private donors have been instrumental in the renewal of the ATA. Breakthrough Listen is managed by the Breakthrough Initiatives, sponsored by the Breakthrough Prize Foundation. The Paul G. Allen Family Foundation provided major support for the design and construction of the ATA, alongside contributions from Nathan Myhrvold, Xilinx Corporation, Sun Microsystems, and other private donors. The ATA was also supported by contributions from the US Naval Observatory and the US National Science Foundation. SZS acknowledges that this material is based upon work supported by the National Science Foundation MPS-Ascend Postdoctoral Research Fellowship under Grant No. 2138147. Participation of JK made possible by SETI Institute REU programme (NSF award #2051007). The authors would also like to thank Ron Maddalena for his help in measuring the sensitivity of the ATA feeds. We acknowledge use of the CHIME/FRB Public Database, provided at https://www.chime-frb.ca/ by the CHIME/FRB Collaboration. We also acknowledge use of the software packages PANDAS (pandas development team 2023), NUMPY (Harris et al. 2020), ASTROPY (Astropy Collaboration 2022), and YOUR (Aggarwal et al. 2020).

DATA AVAILABILITY

The extracted FRB properties are available in the article and in its online supplementary material. The dynamic spectra in archive or filterbank formats will be shared on reasonable request to the corresponding author.

REFERENCES

Agarwal D. et al., 2020, MNRAS, 497, 352
Aggarwal K. et al., 2020, J. Open Source Softw., 5, 2750
Alstott J., Bullmore E., Plenz D., 2014, PloS One, 9, e85777
Astropy Collaboration, 2022, ApJ, 935, 167
Bailes M., 2022, Science, 378, abj3043
Bannister K. W. et al., 2019, Science, 365, 565
Barsdell B. R., 2012, PhD thesis, Swinburne Univ. Technology
Bean B. et al., 2022, PASP, 134, 114501
Beniamini P., Kumar P., 2020, MNRAS, 498, 651
Bhusare Y. et al., 2022, Astron. Telegram, 15806, 1
Bochenek C. D., McKenna D. L., Belov K. V., Kocz J., Kulkarni S. R., Lamb J., Ravi V., Woody D., 2020, PASP, 132, 034202
Bright J. S. et al., 2023, Nat. Astron., 7, 986
CHIME/FRB Collaboration, 2020a, Nature, 582, 351
CHIME/FRB Collaboration, 2020b, Nature, 587, 54
CHIME/FRB Collaboration, 2022, Nature, 607, 256
CHIME/FRB Collaboration, 2023, ApJ, 947, 83

Chamma M. A., Rajabi F., Kumar A., Houde M., 2023, MNRAS, 522, 3036
Clark M. A., La Plante P. C., Greenhill L. J., 2013, The International Journal of High Performance Computing Applications, 27, 178
Clauset A., Shalizi C. R., Newman M. E., 2009, SIAM Rev., 51, 661
Cordes J. M., Chatterjee S., 2019, ARA&A, 57, 417
Cordes J. M., Wasserman I., Hessels J. W. T., Lazio T. J. W., Chatterjee S., Wharton R. S., 2017, ApJ, 842, 35
Dicke R. H., 1954, Phys. Rev., 93, 99
Fedorova V. A., Rodin A. E., 2022, Astron. Telegram, 15713, 1
Feng Y. et al., 2022, Astron. Telegram, 15723, 1
Feng Y. et al., 2023, preprint (arXiv:2304.14671)
Gajjar V. et al., 2018, ApJ, 863, 2
Gajjar V. et al., 2021, AJ, 162, 33
Gajjar V. et al., 2022, ApJ, 932, 81
Gehrels N., 1986, ApJ, 303, 336
Gourdji K., Michilli D., Spitler L. G., Hessels J. W. T., Seymour A., Cordes J. M., Chatterjee S., 2019, ApJ, 877, L19
Harris C. R. et al., 2020, Nature, 585, 357
Herrmann W., 2022, Astron. Telegram, 15691, 1
Hessels J. W. T. et al., 2019, ApJ, 876, L23
Hoshino M., Arons J., 1991, Phys. Fluids B, 3, 818
Hotan A. W., van Straten W., Manchester R. N., 2004, Publ. Astron. Soc. Aust., 21, 302
Houde M., Rajabi F., Gaensler B. M., Mathews A., Tranchant V., 2019, MNRAS, 482, 5492
Jahns J. N. et al., 2023, MNRAS, 519, 666
James C. W., Prochaska J. X., Macquart J. P., North-Hickey F. O., Bannister K. W., Dunning A., 2022, MNRAS, 509, 4775
Kirsten F. et al., 2022, Astron. Telegram, 15727, 1
Kumar P., Shannon R. M., Lower M. E., Bhandari S., Deller A. T., Flynn C., Keane E. F., 2022, MNRAS, 512, 3400
Kumar P. et al., 2023, MNRAS, 526, 3652
Law C. J., ATA Team, 2009, in American Astronomical Society Meeting Abstracts #214. p. 601.05
Law C. J. et al., 2017, ApJ, 850, 76
Li D. et al., 2021, Nature, 598, 267
Lu W., Kumar P., 2018, MNRAS, 477, 2470
Lu W., Piro A. L., 2019, ApJ, 883, 40
Lu W., Kumar P., Zhang B., 2020, MNRAS, 498, 1397
Luo R., Lee K., Lorimer D. R., Zhang B., 2018, MNRAS, 481, 2320
MacKinnon J. G., White H., 1985, J. Econom., 29, 305
Macquart J. P., Ekers R., 2018, MNRAS, 480, 4211
Majid W. A., Pearlman A. B., Nimmo K., Hessels J. W. T., Prince T. A., Naudet C. J., Kocz J., Horiuchi S., 2020, ApJ, 897, L4
Majid W. A. et al., 2021, ApJ, 919, L6
Marcote B. et al., 2020, Nature, 577, 190
McKinven R., CHIME/FRB Collaboration, 2022, Astron. Telegram, 15679, 1
Metzger B. D., Margalit B., Sironi L., 2019, MNRAS, 485, 4091
Michilli D. et al., 2018, Nature, 553, 182
Nimmo K. et al., 2022, Nat. Astron., 6, 393
pandas development team T., 2023, pandas-dev/pandas: Pandas, https://doi.org/10.5281/zenodo.7794821. Last Accessed: 1 October 2023
Pastor-Marazuela I. et al., 2021, Nature, 596, 505
Pearlman A. B., Majid W. A., Prince T. A., Nimmo K., Hessels J. W., Naudet C. J., Kocz J., 2020, ApJ, 905, L27
Perera B. et al., 2022, Astron. Telegram, 15734, 1
Perley R. A., Butler B. J., 2017, ApJS, 230, 7
Petroff E., Hessels J., Lorimer D., 2022, A&AR, 30, 2
Pilia M. et al., 2020, ApJ, 896, L40
Planck Collaboration XIII, 2016, A&A, 594, A13
Platts E. et al., 2021, MNRAS, 505, 3041
Pleunis Z. et al., 2021a, ApJ, 911, L3
Pleunis Z. et al., 2021b, ApJ, 923, 1
Plotnikov I., Sironi L., 2019, MNRAS, 485, 3816
Rajabi F., Chamma M. A., Wyenberg C. M., Mathews A., Houde M., 2020, MNRAS, 498, 4936
Rajwade K. et al., 2022, Astron. Telegram, 15791, 1
Ravi V., 2022, Astron. Telegram, 15716, 1
Ravi V., DSA-110 Collaboration, 2023, in American Astronomical Society Meeting Abstracts. p. 239.01
Ravi V. et al., 2022, ApJ, 949, L3
Ryder S. D. et al., 2022, Science, 383, 294
Sand K. R. et al., 2022, ApJ, 932, 98
Savitzky A., Golay M. J., 1964, Anal. Chem., 36, 1627
Scholz P. et al., 2016, ApJ, 833, 177
Shannon R. M. et al., 2018, Nature, 562, 386
Sheikh S. et al., 2022, Astron. Telegram, 15735, 1
Shin K. et al., 2023, ApJ, 944, 105
Siemion A. P. et al., 2011, ApJ, 744, 109
Sironi L., Plotnikov I., Nättilä J., Beloborodov A. M., 2021, Phys. Rev. Lett., 127, 035101
Sobacchi E., Lyubarsky Y., Beloborodov A. M., Sironi L., 2022, MNRAS, 511, 4766
Spitler L. G. et al., 2016, Nature, 531, 202
van Straten W., Bailes M., 2011, Publ. Astron. Soc. Aust., 28, 1
Wang W.-Y., Yang Y.-P., Niu C.-H., Xu R., Zhang B., 2022, ApJ, 927, 105
Welch J. et al., 2009, Proc. IEEE, 97, 1438
Zhang B., 2020, Nature, 587, 45
Zhang Y. G., Gajjar V., Foster G., Siemion A., Cordes J., Law C., Wang Y., 2018, ApJ, 866, 149
Zhang Y.-K. et al., 2023, ApJ, 955, 142
Zhou D. J. et al., 2022, Res. Astron. Astrophys., 22, 124001

This paper has been typeset from a TEX/LATEX file prepared by the author.